ACS APPLIED MATERIALS & INTERFACES

Research Article

www.acsami.org

SnO_2@PANI Core–Shell Nanorod Arrays on 3D Graphite Foam: A High-Performance Integrated Electrode for Lithium-Ion Batteries

Feng Zhang, Chengkai Yang, Xin Gao, Shuai Chen, Yiran Hu, Huanqin Guan, Yurong Ma, Jin Zhang, Henghui Zhou,* and Limin Qi*

Beijing National Laboratory for Molecular Sciences (BNLMS), College of Chemistry, Peking University, Beijing 100871, China

Supporting Information

ABSTRACT: The rational design and controllable fabrication of electrode materials with tailored structures and superior performance is highly desirable for the next-generation lithium ion batteries (LIBs). In this work, a novel three-dimensional (3D) graphite foam (GF)@SnO_2 nanorod arrays (NRAs)@polyaniline (PANI) hybrid architecture was constructed via solvothermal growth followed by electrochemical deposition. Aligned SnO_2 NRAs were uniformly grown on the surface of GF, and a PANI shell with a thickness of ~40 nm was coated on individual SnO_2 nanorods, forming a SnO_2@PANI core–shell structure. Benefiting from the synergetic effect of 3D GF with large surface area and high conductivity, SnO_2 NRAs offering direct pathways for electrons and lithium ions, and the conductive PANI shell that accommodates the large volume variation of SnO_2, the binder-free, integrated GF@SnO_2 NRAs@PANI electrode for LIBs exhibited high capacity, excellent rate capability, and good electrochemical stability. A high discharge capacity of 540 mAh g^{-1} (calculated by the total mass of the electrode) was achieved after 50 cycles at a current density of 500 mA g^{-1}. Moreover, the electrode demonstrated superior rate performance with a discharge capacity of 414 mAh g^{-1} at a high rate of 3 A g^{-1}.

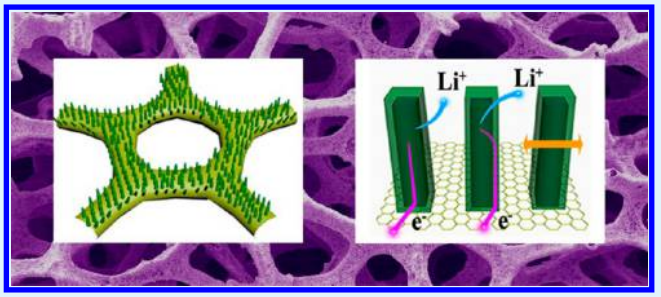

KEYWORDS: *graphite foam, SnO_2 nanorod arrays, PANI, integrated electrode, lithium-ion batteries*

1. INTRODUCTION

Since Sony introduced the first version in the early 1990s, rechargeable lithium ion batteries (LIBs) have rapidly gained momentum owing to their high energy density, high working potential, long cycling lifespan, and good environmental compatibility.[1−3] However, the current LIBs utilize graphite as the anode with a relatively low specific capacity of 372 mAh g^{-1}, which hinders their practical applications in the fields of electrical vehicles and smart grids.[4−6] Extensive efforts have been dedicated to investigating SnO_2-based materials as a potential candidate for replacing graphite owing to their high theoretical specific capacity (1494 mAh g^{-1}), which is almost four times higher than that for graphite.[7,8] Unfortunately, bulk SnO_2 suffers from huge volume change (~300%) that leads to the pulverization of electrode and the formation of unstable solid electrolyte interface (SEI), which is in turn detrimental to capacity retention.[9] Besides, SnO_2 is a semiconductor material with low electron conductivity that usually results in poor rate capability.[10]

Recent progress has shown that the fabrication of SnO_2-based nanomaterials can simultaneously achieve a higher specific capacity and a better rate capability,[11−17] because the nanosized SnO_2 offers decreased ion diffusion lengths, large electrolyte contact area, and enhanced interfacial kinetics. Nevertheless, severe self-aggregation of SnO_2 nanocrystals tends to cause the loss of electrical contact between active materials and current collector, resulting in rapid capacity fading. Consequently, the fabrication of hybrid architectures combining SnO_2 with a variety of conductive materials has been widely investigated, aimed at improving the thermodynamic stability by avoiding direct contact of SnO_2 nanocrystals upon cycling.[18−22] Particularly, in situ characterization results have shown that one-dimensional (1D) SnO_2 nanomaterials have a relatively high structural stability and the coating strategy is an effective method for improving the cycling performance.[23] Among various conductive materials, carbonaceous nanomaterials (such as porous carbons, carbon nanotubes, and graphene) have been evidenced to be a promising candidate with good mechanical property and high conductivity.[24−33] The combination of carbonaceous nanomaterials and SnO_2 often exhibits notable synergetic effect with enhanced electrochemical performance.

Despite improved performance of SnO_2-based hybrid electrodes, it is still a challenge to realize their real-world applications. In particular, the indispensable additives (such as conductive agents and binders) during electrode manufacture processes have no contribution to the whole capacity, and the increased grain boundaries result in large interfacial transfer

Received: December 11, 2016
Accepted: March 1, 2017
Published: March 1, 2017

DOI: 10.1021/acsami.6b15880
ACS Appl. Mater. Interfaces 2017, 9, 9620–9629

resistance causing adverse effect on the rate capability.[34,35] To address this obstacle, a novel electrode fabrication strategy has been designed to construct integrated LIBs electrodes without additives via filling SnO_2 nanomaterials into a porous, self-supported and lightweight carbonaceous matrix (such as paper, film, and foam). For example, Hu et al. fabricated a binder-free anode through electrodepositing SnO_2 nanocrystals on self-supported carbonized filter paper.[36] The as-prepared anode was directly used as working electrode in LIB cells and demonstrated enhanced electrochemical properties. Xia et al. further encapsulated SnO_2 nanocrystals into an N-doped carbon nanofiber film by a facile electrospinning strategy.[10] The free-standing film exhibited higher specific capacity and better cycling stability compared with SnO_2 nanoparticles. Beyond that, SnO_2-graphene foam,[37] graphene/SnO_2 nanocomposite paper,[38] SnO_2 nanorod/graphene composite film,[39] carbon nanotube/SnO_2 paper,[40] SnO_2/carbon nanofiber composites,[41] and carbon foam/SnO_2 composite[42] were also produced. All these integrated electrodes showed considerably improved specific capacities with respect to the total mass of the electrode; nevertheless, the rate capabilities are still unsatisfying and a reasonable strategy to improve the rate performance would be employing other carbonaceous materials with higher conductivity, such as pristine graphene and graphite.

Recently, three-dimensional (3D) graphite foam (GF, also called graphene foam) derived from chemical vapor deposition (CVD), which has a high conductivity and porosity that guarantee both fast charge transport and good contact between active materials and electrolyte, has been regarded as an excellent backbone for direct deposition of active materials.[43−49] Therefore, constructing SnO_2 nanostructures on GF may provide an exciting platform for enhancing the rate capability of the SnO_2-based integrated electrodes. However, to the best of our knowledge, integrated 3D GF@SnO_2 electrodes have not been realized yet possibly due to the difficulty in the deposition of SnO_2 nanostructures on the inert surface of GF. In our recent work, a unique kinetics-controlled growth method was developed for the fabrication of aligned mesocrystalline SnO_2 nanorod arrays on arbitrary inert substrates, such as titanium foil,[50] carbon nanotubes,[51] and reduced graphene oxide.[52] Moreover, the core−shell nanostructures consisting of a metal oxide core coated by a conductive polymer shell have demonstrated enhanced electron conductivity of the electrode due to the unique electrical characters and good mechanical properties of conductive polymers.[20,21,45,53−55] In this work, we fabricated a mesocrystalline SnO_2 nanorod arrays-based integrated 3D anode through the growth of SnO_2 nanorod arrays (NRAs) on 3D GF current collector (denoted as GF@SnO_2 NRAs), followed by coating SnO_2 nanorods with a uniform thin shell of the conductive polymer polyaniline (PANI) through electrochemical deposition (ED) to further enhance the electrochemical property. The resulting integrated electrode (denoted as GF@SnO_2 NRAs@PANI) exhibited a high specific capacity of 540 mAh g^{-1} (calculated by the total mass of the electrode) at a current density of 500 mA g^{-1} after 50 cycles, which is much higher than that for the commercial anode of graphite with respect to the total electrode mass. Furthermore, the electrode demonstrated superior rate performance with a discharge capacity of 414 mAh g^{-1} at a high rate of 3 A g^{-1}.

2. EXPERIMENTAL SECTION

2.1. Materials. Nickel foam (>99.8%) was purchased from Shanxi Lizhiyuan Battery Material Co., Ltd. $SnCl_4{\cdot}5H_2O$ (>99.0%) was from Sinopharm Chemical Reagent Co., Ltd. NaBr (>99.0%), sulfuric acid (95.0−95.9%), and aniline (99.5%) were from Xilong Chemical Co., Ltd. Glacial acetic acid (99.5%) and ethanol (99.7%) were from Beijing Tongguang Fine Chemicals Company.

2.2. Synthesis of 3D GF. The synthesis of 3D GF was achieved by chemical vapor deposition (CVD) according to the reported method.[56] In a typical process, the nickel foam plate (1.7 mm in thickness) as the scaffold template was cut into 0.8 × 0.8 cm^2 and placed directly in a tube furnace. The nickel foams were heated to 900 °C under the gas flow of Ar (280 sccm) and H_2 (20 sccm) atmosphere and annealed for 15 min for the purpose of eliminating the thin oxide layer on the surface. Then, a small amount of ethanol was introduced into the reaction tube by Ar (170 sccm) and H_2 (40 sccm) flow under ambient pressure. After reaction for 30 min, the tube was cooled to room temperature under the protection atmosphere of Ar (280 sccm) and H_2 (20 sccm). The size of 3D GF could be easily adjusted by changing the size of nickel foam substrate. The free-standing 3D GF (ca. 0.6 mg cm^{-2}) was obtained by etching the nickel template in 3 M hydrochloric acid solution at 80 °C for 5 h to thoroughly dissolve the nickel template.

2.3. Fabrication of GF@SnO_2 NRAs. The obtained free-standing 3D GF was directly used as a substrate for the growth of SnO_2 NRAs by the solvothermal synthesis in a mixed solvent system consisting of ethanol, acetic acid, and water. Typically, 3 mmol NaBr and 0.2 mmol $SnCl_4{\cdot}5H_2O$ were dissolved in 1 mL of water and 7 mL of glacial acetic acid, respectively. Then, these two clear solutions were mixed followed by adding 1 mL of ethanol into the mixture under continuous stirring for 10 min. The obtained pale yellow solution was transferred into a Teflon-lined stainless steel autoclave (25 mL). The 3D GF (0.8 × 0.8 × 1.7 cm^3) was immersed into the reaction solution. The autoclave was kept at 200 °C for 24 h. After the autoclave was cooled to room temperature, the sample was taken out from the autoclave and rinsed with water and ethanol alternately for three times. The GF@SnO_2 NRAs was obtained after annealing at 450 °C in air for 30 min to remove the residual organics.

2.4. Preparation of GF@SnO_2 NRAs@PANI. A PANI shell was coated onto the SnO_2 nanorods by an electrochemical deposition (ED) technique. Aniline was distilled under reduced pressure and stored in the sealed state at 4 °C. The electrolyte was obtained by adding 0.5 mL of aniline into 100 mL 0.1 M sulfuric acid. The ED of PANI was carried out in a three-electrode system with the Ag/AgCl electrode as the reference electrode, platinum foil as the counter electrode, and the GF@SnO_2 NRAs as the working electrode. A CHI660C electrochemical workstation was utilized for electrodepositing PANI through a cyclic voltammetry (CV) method at a scan rate 30 mV s^{-1} between −0.2 and 1.6 V for 1200 s, leading to a mass ratio of PANI of ca. 20%. As a control sample, the ED for 600 s was also conducted, and a mass ratio of PANI of ca. 10% was achieved (the weight change of the electrode was determined by measuring the mass of the hybrid structure before and after ED).

2.5. Characterizations. The structure of the obtained samples was characterized by X-ray diffraction (XRD, Rigaku Dmax-2000, Cu Kα radiation) and Raman spectroscopy (Horiba HR800). Transmission electron microscopy (TEM, FEI Tecnai F30, 300 kV) and field-emission scanning electron microscopy (SEM, Hitachi S4800, 5 kV) equipped with energy-dispersive X-ray spectroscopy (EDS) were used to study the morphology and microstructure of the samples. Thermogravimetric analysis (TGA) was carried out on a Q50 thermoanalyzer with air as the carrier gas at a heating rate of 10 °C min^{-1}.

2.6. Electrochemical Measurements. The three samples (GF, GF@SnO_2 NRAs, and GF@SnO_2@PANI) were directly utilized as binder-free anodes for LIB. The electrode was assembled in a 2032 coin cell with pure lithium foil as the counter electrode, Celgard 2400 as the separator, and 1 M lithium hexafluorophosphate ($LiPF_6$) in a mixture of ethylene carbonate (EC), ethyl methyl carbonate (EMC),

DOI: 10.1021/acsami.6b15880
ACS Appl. Mater. Interfaces 2017, 9, 9620−9629

and dimethyl carbonate (DMC) (1:1:1 by volume) as the electrolyte in a glovebox filled with argon. The electrochemical performance was conducted by utilizing a LAND CT2001A battery test system at room temperature. The assembled batteries were discharged and charged at a constant current with a cutoff voltage window of 3.0 and 0.05 V (vs Li^+/Li). A CV autolab (Eco Chemie, PGSTAT302N) was used for the cyclic voltammetry (CV) tests. An electrochemical workstation (CHI660D, Shanghai Chenhua) was utilized for the electrochemical impedance spectroscopy (EIS) measuremets in the frequency range 10^{-2}–10^5 Hz.

3. RESULTS AND DISCUSSION

Figure 1 illustrates the entire fabrication process of the integrated GF@SnO_2 NRAs@PANI electrode. Specifically,

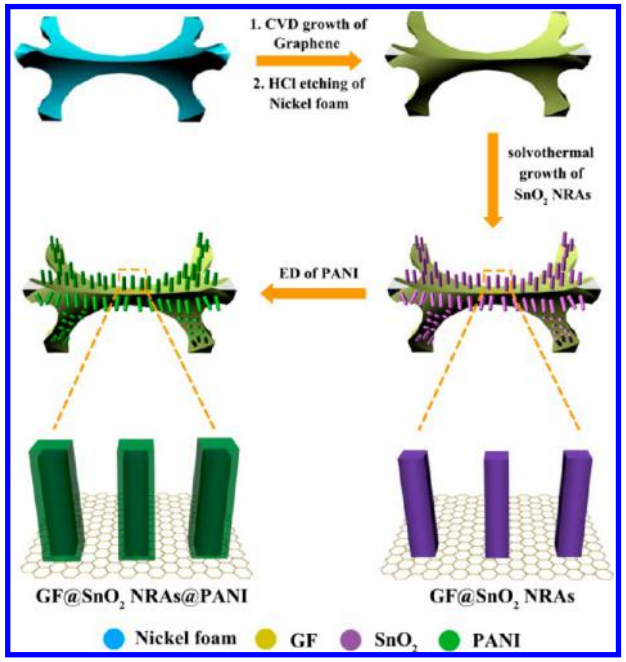

Figure 1. Schematic illustration of the fabrication process of GF@SnO_2 NRAs@PANI.

the 3D porous GF was first synthesized via a CVD method followed by hydrochloric acid etching of the template nickel foam. Then, a facile solvothermal procedure was utilized for growth of aligned mesocrystalline SnO_2 NRAs on 3D porous GF in a mixed solvent system consisting of ethanol, acetic acid, and water to form GF@SnO_2 NRAs. Finally, a thin layer of conductive polymer PANI shell was coated on individual SnO_2 nanorods via an ED method to obtain the 3D GF@SnO_2 NRAs@PANI electrode. Notably, the thickness of the PANI layer could be easily controlled by adjusting the electrodeposition time. In particular, the electrode after ED for 600 s had a PANI layer thickness of ~20 nm, which is denoted as GF@SnO_2NRAs@PANI-20, while the electrode after ED for 1200 s had a PANI layer thickness of ~40 nm, which is denoted as GF@SnO_2NRAs@PANI-40.

The morphology of the obtained GF, GF@SnO_2 NRAs, and GF@SnO_2 NRAs@PANI-40 was systematically investigated by SEM, as shown in Figure 2. The as-prepared GF holds similar characteristics of the nickel foam template with a 3D continuous and interconnected network, showing individual skeleton branches about 50–100 μm in length and 50 μm in width and a variety of macropores with a diameter of 100–500 μm (Figure 2a). Closer SEM observation of a broken branch suggests a hollow structure (Figure 2b), indicating that the nickel template was completely etched. The high-magnification SEM image presented in Figure 2c indicates that there are ripples and wrinkles on the surface of GF, but no obvious cracks are observed, which would be favorable for electron transport. It is worth noting that the prepared GF plate ~1.7 mm in thickness has a low areal density of ~0.6 mg cm^{-2}, which is much lower than that for the pristine template nickel foam (~30 mg cm^{-2}). Therefore, such a lightweight 3D GF plate as a self-supported current collector would be beneficial for the improvement of the energy density of the whole electrode. After the solvothermal procedure, the 3D GF was uniformly coated by aligned SnO_2 NRAs, as shown in Figure 2d–f. Particularly, the growth of SnO_2 nanoarrays did not destroy the skeleton and macroporous architectures of the 3D GF (Figure 2d). The SnO_2 NRAs mainly grew vertically on the outer surface of the GF, and only few nanorods were detected on the inner surface (Figure 2e). The NRAs have a length of ~600 nm, and the individual SnO_2 nanorod is needlelike with a diameter about 50–100 nm (Figure 2f). After the introduction of the PANI layer via electrodeposition, the 3D skeleton of GF was still preserved and the width of the nanorod increased to ~150 nm (Figure 2g,h).

The three representative samples GF, GF@SnO_2 NRAs, and GF@SnO_2 NRAs@PANI-40 were further characterized by TEM and high-resolution TEM (HRTEM). Figure 3a shows the intrinsic ultrathin slice and wrinkles of the GF, and a hexagonal pattern characteristic of graphitic carbon can be observed from the related selected area electron diffraction (SAED) pattern. The GF is composed of a few tens of graphene layers, and the measured lattice spacing of ~0.34 nm can be ascribed to the (002) plane graphitic carbon (Figure 3b). Figure 3c shows the low-magnification TEM image of an individual SnO_2 nanorod together with the corresponding SAED pattern characteristic of single crystalline tetragonal rutile SnO_2, suggesting that the SnO_2 nanorod is oriented along the [001] direction. Furthermore, the inset in Figure 3c clearly shows that the SnO_2 nanorod is composed of a bunch of rod-like subunits, indicating that the whole SnO_2 nanorod is actually mesocrystalline with some apparent interspaces.[50] The HRTEM image in Figure 3d shows that the measured lattice spacings of 0.32 and 0.34 nm correspond to the (001) and (110) planes of the rutile SnO_2, respectively, confirming that the primary SnO_2 nanorod is a single crystal elonated along the [001] orientation. After the electrodeposition of PANI, the SnO_2 nanorod was tightly coated with a uniform PANI layer with a thickness of ~40 nm (Figure 3e). The HRTEM image shown in Figure 3f reveals that the PANI layer is amorphous whereas the primary SnO_2 nanorod preserves its single-crystalline structure with the (001) and (110) planes well observed. Our preliminary experimental results showed that the GF@SnO_2 NRA@PANI architecture with a thinner PANI layer could be achieved by shortening the ED process. For example, the GF@SnO_2 NRA@PANI-20 electrode with a PANI shell thickness of ~20 nm was obtained by decreasing the ED time to 600 s (Figure S1).

The XRD and Raman characterizations of GF, GF@SnO_2 NRAs, and GF@SnO_2 NRAs@PANI-40 are shown in Figure 4a. The GF exhibits two diffraction peaks at 26.2° and 53.9°, which are corresponding to the (002) and (004) planes of graphitic carbon (JCPDS card no. 75-1621), respectively. In contrast, all the visible diffraction peaks of GF@SnO_2 NRAs can be assigned to tetragonal rutile SnO_2 (JCPDS card no. 41-

DOI: 10.1021/acsami.6b15880
ACS Appl. Mater. Interfaces 2017, 9, 9620–9629

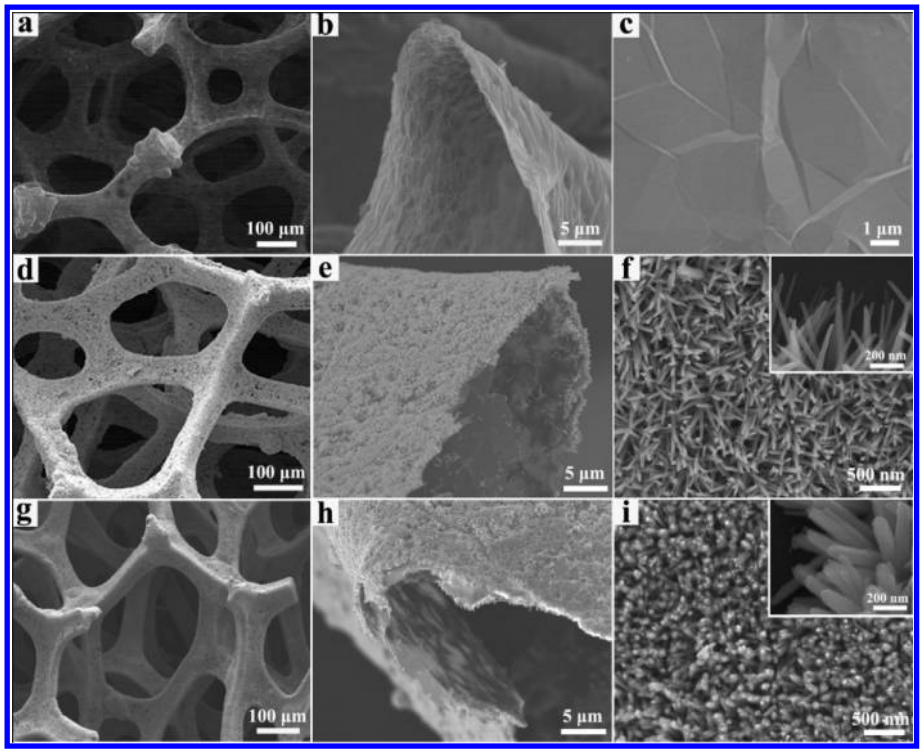

Figure 2. SEM images of (a–c) GF, (d–f) GF@SnO_2 NRAs, and (g–i) GF@SnO_2 NRAs@PANI-40. Panels (b), (e), and (h) are the cross section images of the broken GF branch, and the insets in (f) and (i) show the magnified images.

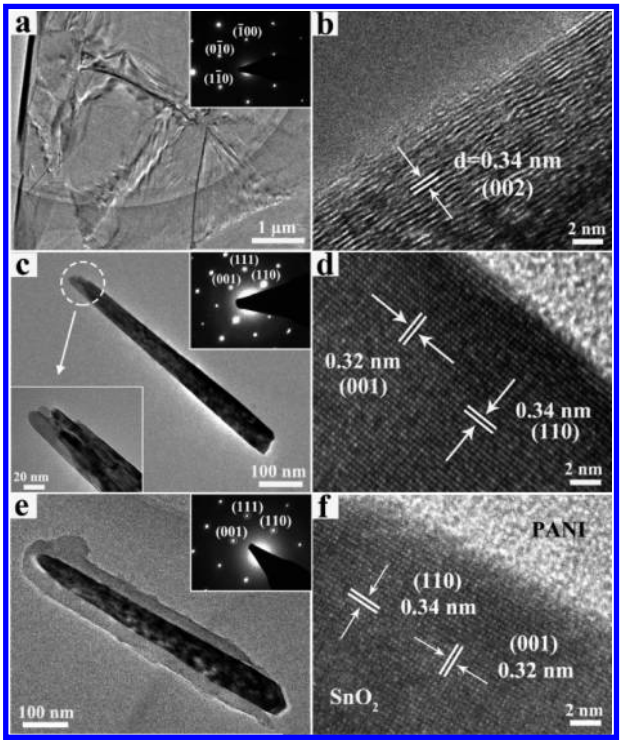

Figure 3. TEM (a,c,e) and HRTEM (b,d,f) images of (a,b) GF, (c,d) GF@SnO_2 NRAs, and (e,f) GF@SnO_2 NRAs@PANI-40. The insets in (a), (c), and (e) show the corresponding SAED patterns. An enlarged image of the tip of the SnO_2 nanorod is also shown in the inset of (c).

1445), indicating the formation of pure phase SnO_2. After the electrodeposition of PANI, the XRD pattern remains essentially unchanged, which is consistent with the TEM observation that

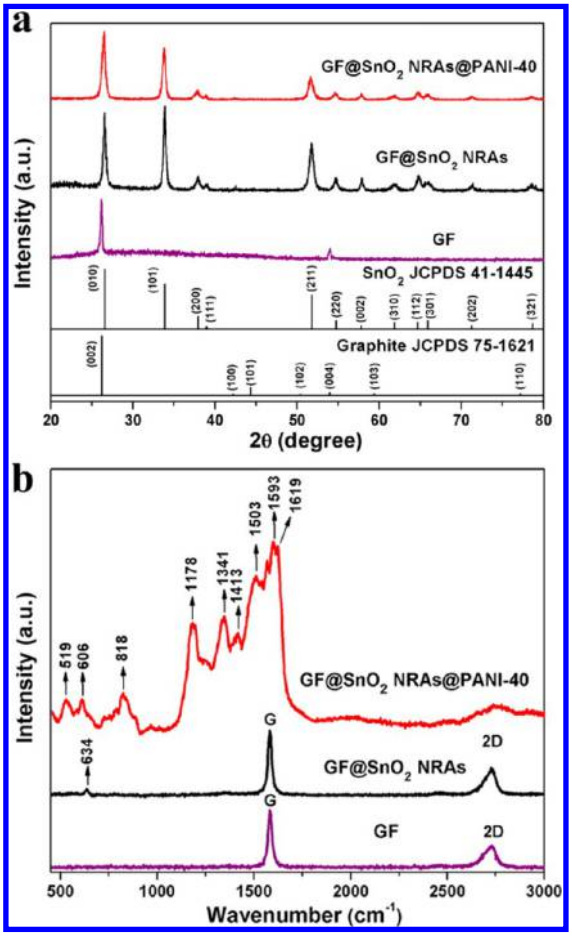

Figure 4. (a) XRD patterns and (b) Raman spectra of GF, GF@SnO_2 NRAs and GF@SnO_2 NRAs@PANI-40.

DOI: 10.1021/acsami.6b15880
ACS Appl. Mater. Interfaces 2017, 9, 9620–9629

an amorphous PANI layer was coated on the SnO_2 nanorods. Additional information concerning the chemical composition of the three samples was obtained by Raman characterization. Raman spectra shown in Figure 4b exhibits two characteristic peaks of graphene at 1581.8 and 2730.8 cm^{-1}, which can be ascribed to the G and 2D bands.[57] It has been reported that the intensity ratio of the 2D and G bands (I_{2D}/I_G) is usually utilized to determine the layer number of graphene, and the I_{2D}/I_G value of the defect-free single-layer graphene equals to 2.[58] Generally, this value decreases with the increase of graphene layer numbers. In this work, the GF exhibits an I_{2D}/I_G value of 0.5, indicating that the GF consisting of multilayer graphene with the properties similar to graphite. Therefore, an appropriate definition of GF should be graphite foam rather than graphene foam. In addition, the absence of a Raman band at 1350 cm^{-1} (D band) implies that the as-prepared GF is of high quality,[44] which would guarantee fast electron transport. It is indicated that the structure of GF was not destroyed after annealing at 450 °C in air, which is consistent with the reported result.[59] For GF@SnO_2 NRAs, a small band is found at 634 cm^{-1}, which can be attributed to the A_{1g} vibration mode of Sn−O−Sn bonds.[60] The Raman spectrum of GF@SnO_2 NRAs@PANI shows a series of peaks characteristic of PANI.[61] The peaks at 519, 606, 818, and 1178 cm^{-1} correspond to the phenazine-like segment, benzenoid ring deformation, symmetric benzenoid ring stretching, and in plane C−H bending of the quinine ring, respectively. The peaks at 1341 and 1413 cm^{-1} are associated with the vibration of semiquinone radical and C−C stretching, respectively. Characteristic of C═N stretching vibration of the quinine ring is situated at 1503 and 1593 cm^{-1}. The peak at 1617 cm^{-1} originates from C−C stretching of the benzenoid ring.

Furthermore, the existence of the PANI shell was identified by SEM and TEM observations coupled with EDS analysis (Figure 5). The SEM image, EDS spectrum, and EDS elemental imaging of a skeleton trunk of GF@SnO_2 NRAs@PANI-40 confirm the uniform distribution of N element from PANI, indicating the formation of SnO_2@PANI core−shell structure (Figure 5a−f). A high-angle annular dark field-scanning transmission electron microscopy (HAADF-STEM) image is shown in Figure 5g, and the EDS line scanning of a single nanorod is shown in Figure 5h. It can be seen that the content of C element is enriched outside the SnO_2 nanorod (the spectrum of N element is not shown because of the weak signal associated with the low content), while the Sn and O elements are present only inside the SnO_2 nanorod, indicating that a PANI shell has been coated on the surface of the SnO_2 nanorod. Therefore, it can be concluded that a unique integrated electrode GF@SnO_2 NRAs@PANI-40 consisting of SnO_2@PANI core−shell nanoarrays grown on 3D GF was successfully fabricated, which could be expected to exhibit good cyclability, high capacity, and rate capability for LIBs.

The produced integrated electrode GF@SnO_2 NRAs@PANI-40 can be directly used as a binder-free LIB anode without an additional current collector. Detailed electrochemical tests were carried out to investigate the lithium ion storage performance of the integrated electrode. The cyclic voltammetry (CV) curves of GF@SnO_2 NRAs@PANI-40 scanned at 0.5 mV s^{-1} in the voltage window from 0.05 to 3 V (vs Li^+/Li) during the first three charge/discharge cycles are presented in Figure 6a. The simplified electrochemical reaction of SnO_2 could be separated into two steps:[8]

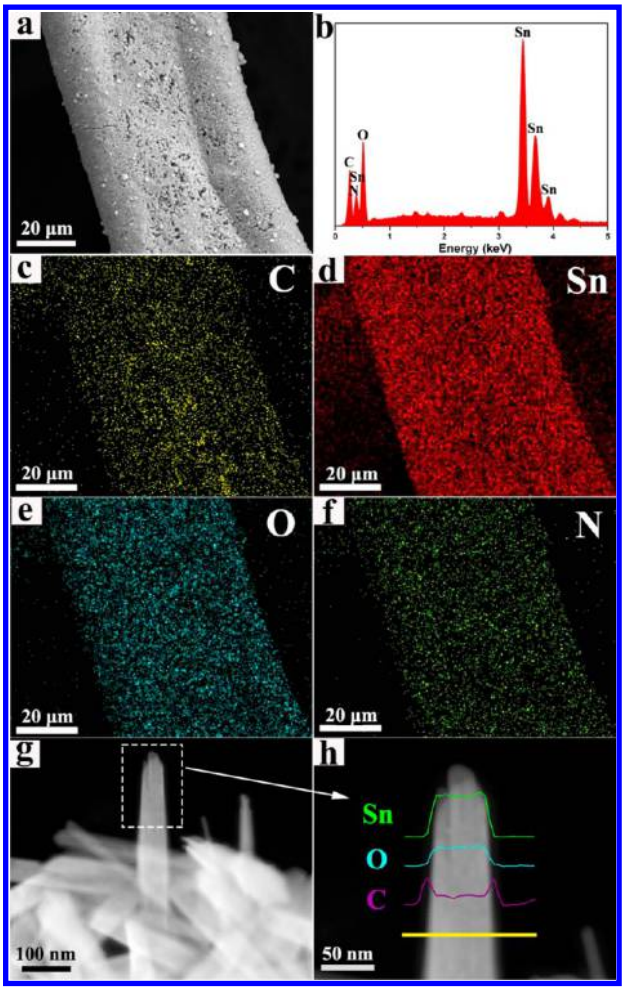

Figure 5. (a) SEM image, (b) EDS spectrum, and (c−f) EDS elemental mapping of GF@SnO_2 NRAs@PANI-40. (g) HAADF-STEM image of GF@SnO_2 NRAs@PANI-40 and (h) EDS line scan of a single nanorod along the yellow line.

$$SnO_2 + 4e^- + 4Li^+ \rightarrow Sn + 2Li_2O \quad (1)$$

$$Sn + nLi^+ + 4.4e^- \leftrightarrow Li_nSn \quad (0 \le n \le 4.4) \quad (2)$$

SnO_2 is first converted to metallic Sn and amorphous Li_2O, and then a highly reversible alloying/dealloying reaction between Sn and Li^+ occurred, resulting in a high theoretical gravimetric capacity of 1494 mAh g^{-1}. As shown in Figure 6a, two pairs of cathodic/anodic peaks arising from the alloying/dealloying process of nonstoichiometric Li_nSn ($0 \le n \le 4.4$) are detected at potentials of 0.05 and 0.65 V.[11] The second cathodic/anodic peaks can be observed at 0.68 and 1.34 V. The sharp peak at 0.68 V in the first cathodic scan represents the reduction of SnO_2 to metallic Sn and amorphous Li_2O.[62] The CV curves of the second and third cycles almost overlap, implying good cycling stability of the electrode. It is noteworthy that two peaks located at 0.1 and 0.27 V can be observed from the CV curves, which correspond to the lithiation/delithiation of graphite foam in the testing potential range, respectively.[48] Actually, pure GF has a certain capacity for lithium storage (Figure S2), indicating that GF would have a contribution to the whole capacity of the integrated electrode. There are no apparent peaks corresponding to PANI in the CV profiles, indicating that the PANI shell would contribute neglectable capacity in the whole electrode. Figure 6b displays the

DOI: 10.1021/acsami.6b15880
ACS Appl. Mater. Interfaces 2017, 9, 9620−9629

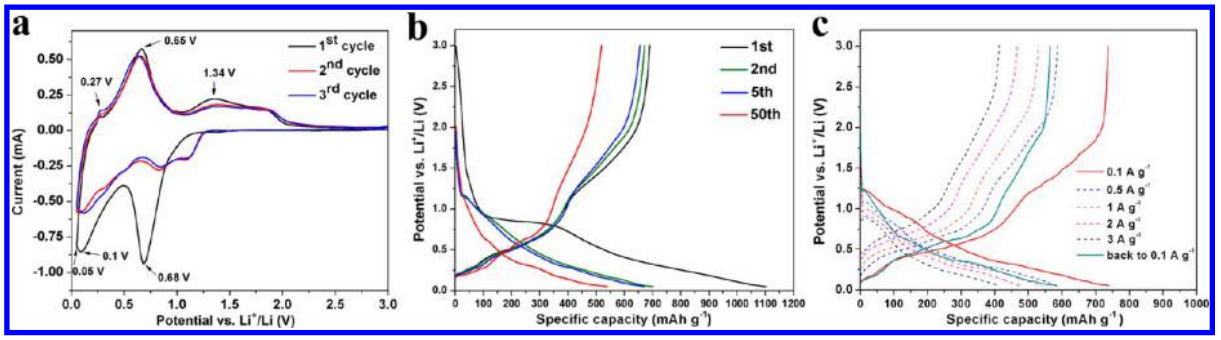

Figure 6. Electrochemical performance of GF@SnO_2 NRAs@PANI-40. (a) Cyclic voltammetry curves with a scan rate of 0.5 mV s^{-1} of the initial three cycles. (b) Galvanostatic charge/discharge profiles of 1st, 2nd, 5th, and 50th cycles. (c) Charge/discharge profiles at 0.1, 0.5, 1, 2, 3, and 0.1 A g^{-1} indicating the rate capability.

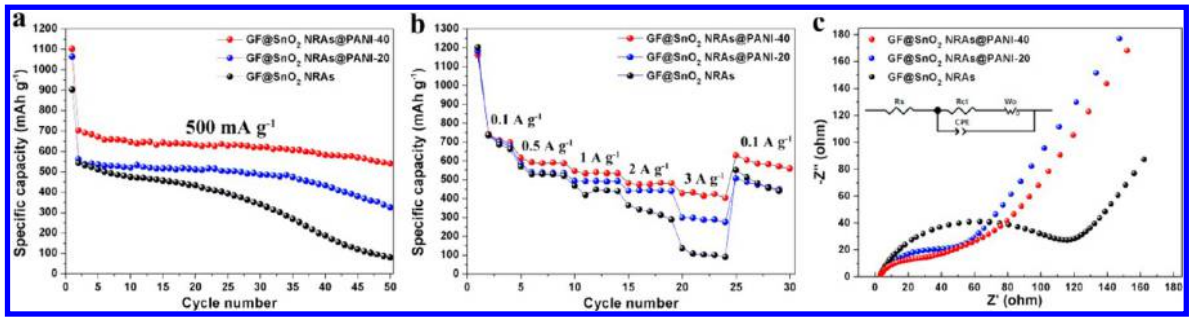

Figure 7. Comparative electrochemical properties of GF@SnO_2 NRAs, GF@SnO_2 NRAs@PANI-20, and GF@SnO_2 NRAs@PANI-40. (a) Cycling performance at a current density of 500 mA g^{-1}. (b) Rate capability at different discharge current densities. (c) Nyquist plots in the frequency range of 10^{-2}–10^5 Hz.

representative Galvanostatic discharge profiles of GF@SnO_2 NRAs@PANI-40 at a current density of 500 mA g^{-1}, where the specific capacity was calculated based on the total electrode mass. The initial discharge capacity of the electrode is 1102 mAh g^{-1} with respect to the total electrode mass. Such a high initial discharge capacity might be attributed to the 1D mesocrystalline SnO_2 with many small subunits and high surface area for interfacial lithium loading, and the conductive graphitic backbone and PANI shell that promote electron transport. The charge capacity in the first cycle is 690 mAh g^{-1}, corresponding to an initial Coulombic efficiency of 63%. The capacity loss may be ascribed to the irreversible reduction of SnO_2 to metallic Sn, and the decomposition of electrolyte to form a solid electrolyte interface (SEI) film.[51] The Coulombic efficiency reaches more than 97% after several cycles The rate performance of GF@SnO_2 NRAs@PANI-40 is shown in Figure 6c, which suggest that discharge capacities of 740, 587, 539, 476, and 414 mAh g^{-1} were delivered at the current densities of 0.1, 0.5, 1, 2, and 3 A g^{-1}, respectively. When the current density goes back to 0.1 A g^{-1}, the discharge capacity recovers to 585 mAh g^{-1}, indicating excellent rate capability. It is noteworthy that such a rate capability is considerably higher than those for many SnO_2-carbon nanocomposites such as hollow core–shell SnO_2/C fibers[24] and hierarchical porous reduced graphene oxide/SnO_2 networks,[32] which exhibited discharge capacities (with respect to the active materials) of 267 and 190 mAh g^{-1} at 3 A g^{-1}, respectively.

Comparative investigation of the lithium storage performance of GF@SnO_2 NRAs, GF@SnO_2 NRAs@PANI-20, and GF@SnO_2 NRAs@PANI-40 were carried out to reveal the effects of the PANI coating. As shown in Figure 7a, after 50 cycles at a current density of 500 mA g^{-1}, the discharge capacity of GF@SnO_2 NRAs@PANI-40 was stable at 540 mAh g^{-1} with respect to the total electrode mass, which is still considerably higher than the theoretical capacity of graphite (372 mAh g^{-1}), let alone the capacity of commercial graphite calculated by the total electrode mass including copper current collector, conductive carbon black and binders.[46] In contrast, GF@SnO_2 NRAs without PANI coating showed poor cycling stability with severe capacity decay under the same testing condition. After 50 cycles, the GF@SnO_2 NRAs electrode delivered low discharge capacity of 80 mAh g^{-1}. With a thin PANI coating layer (~20 nm), the GF@SnO_2 NRAs@PANI-20 electrode demonstrated improved cycling performance with a capacity of 325 mAh g^{-1} kept after 50 cycles, which, however, is still considerably lower than that for the GF@SnO_2 NRAs@PANI-40 electrode with a thicker PANI layer (~40 nm). It may be reasonably expected that a better cycling performance would be achieved for GF@SnO_2 NRAs@PANI at a smaller rate. As a simple demonstration, the cycling performance of the GF@SnO_2 NRAs@PANI-40 electrode at a current density of 100 mA g^{-1} was measured (Figure S3). As expected, a high reversible capacity of ~750 mAh g^{-1} was delivered after 30 cycles at 100 mA g^{-1}, which is considerably higher than that delivered at 500 mA g^{-1} (~620 mAh g^{-1}). Thermogravimetric analysis (TGA) showed that the weight ratio of SnO_2 in the GF@SnO_2 NRAs electrode accounted for ~77% (Figure S4), indicating the contents of GF and PANI in the GF@SnO_2 NRAs@PANI-40 electrode account for ~18% and ~20%, respectively. Since the areal density of the GF plate is ~0.6 mg cm^{-2}, the mass loading of SnO_2 in the integrated electrode was estimated to be ~2.0 mg cm^{-2}. If both GF and SnO_2 were taken into consideration, the mass loading of active materials is ~2.6 mg cm^{-2}. As the electrode was pressed during the normal assembly process of coin cells, the as-prepared GF@SnO_2 NRAs@PANI-40 plate ~1.7 mm in thickness became thinner

DOI: 10.1021/acsami.6b15880
ACS Appl. Mater. Interfaces 2017, 9, 9620–9629

when it was pressed into the final electrode, which was estimated to have a thickness of ~100 μm (Figure S5). Therefore, after 50 cycles at 500 mA g^{-1}, the volumetric capacity was still maintained at 162 mAh cm^{-3} based on the total volume of the electrode.

While GF@SnO_2 NRAs and GF@SnO_2 NRAs@PANI-20 showed discharge capacities of 103 and 287 mAh g^{-1} at a high current density of 3 A g^{-1}, respectively, GF@SnO_2 NRAs@PANI-40 exhibited superior rate capability with a capacity of 414 mAh g^{-1} retained at the discharge rate of 3 A g^{-1}, as shown in Figure 7b. If the capacity based on the total electrode mass is considered, the rate capability of the GF@SnO_2 NRAs@PANI-40 electrode is higher than those for most of the reported binder-free anodes based on SnO_2-carbon nanomaterial hybrids,[36−42] and comparable to that for the SnO_2/N-doped carbon nanofiber films[10] (Table S1). Notably, the GF@SnO_2 NRAs@PANI-40 exhibited a considerably higher rate capability compared with the core−shell SnO_2-PANI nanorod arrays grown on nickel foam (312 mAh g^{-1} at 3 A g^{-1}),[20] which can be largely attributed to the lightweight character of the graphite form. Therefore, the current GF@SnO_2 NRAs@PANI-40 electrode may represent a promising candidate to substitute conventional graphite anode for the next generation LIBs due to its high capacity and excellent rate capability.

The EIS technology is an effective method to investigate the charge transfer kinetics occurring at the electrolyte/electrode interface. The measured Nyquist plots of the three electrodes are shown in Figure 7c, which shows that each plot comprises of a semicircle and a sloping line. The diameter of the semicircle in high-frequency field is associated with the charge transfer resistance (R_{ct}) on electrolyte/electrode interface, and the sloping low-frequency line is known as Warburg resistance that represents the resistance corresponding to diffusion of lithium ions into the active materials in electrode.[63] According to the equivalent circuit model, the GF@SnO_2 NRAs@PANI-40 electrode exhibited a much smaller R_{ct} (20.14 Ω) compared with the GF@SnO_2 NRAs electrode (100.5 Ω), indicating an accelerated charge transfer rate due to the homogeneous coating of the PANI shell. The GF@SnO_2 NRAs@PANI-20 electrode exhibited a slightly larger R_{ct} (34.8 Ω) than that of the GF@SnO_2 NRAs@PANI-40 electrode because of the thinner PANI layer. In addition, the lithium diffusion coefficient D was also analyzed to clearly illustrate the influence of thickness of the PANI layer on the electrochemical properties. The D value was calculated from the sloping lines in the Warburg region.[64] After a linear fitting of the variation of Z_{re} versus the reciprocal square root of the angular frequency ω, the GF@SnO_2 NRAs@PANI-40 electrode exhibited a smaller slope compared with the GF@SnO_2 NRAs@PANI-20 electrode (Figure S6), indicating a larger lithium diffusion coefficient D, which suggests that a thicker PANI shell was more favorable for the lithium diffusion process.

The improved electrochemical performance of the integrated GF@SnO_2 NRAs@PANI-40 electrode could be ascribed to the synergetic effect of 3D GF, SnO_2 NRAs, and PANI (Figure 8): First, the formation of the SnO_2@PANI core−shell nanorod structure on 3D GF can buffer the huge volume change of SnO_2 nanorods during lithiation/delithiation process owing to the protective PANI layer as well as the GF substrate. In contrast, the SnO_2 nanrods without the PANI shell tended to experience severe crack and pulverization. The SEM, TEM, and HRTEM observations of fully discharged GF@SnO_2 NRAs and GF@SnO_2 NRAs@PANI-40 after 50 cycles at a current density

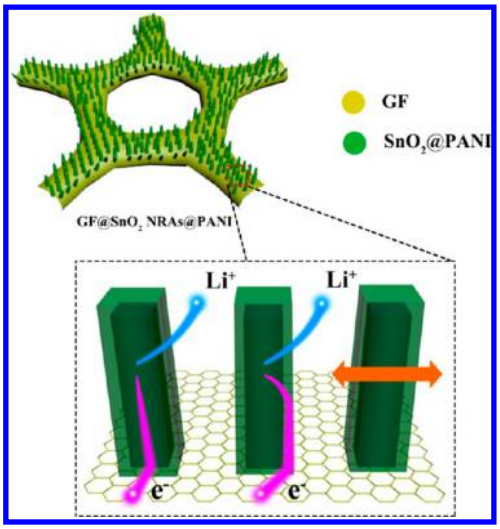

Figure 8. Schematic illustration of the charge/discharge process of integrated GF@SnO_2 NRAs@PANI electrode.

of 500 mA g^{-1} confirmed that the integrity of the SnO_2@PANI core−shell nanorods was retained whereas the SnO_2 nanorods without the PANI shell endured serious destruction (Figure S7). It may be noted that the HRTEM image of GF@SnO_2 NRAs@PANI-40 after 50 cycles exhibited clear lattice fringes with a spacing of 0.29 nm, which is consistent with the (200) plane of Sn crystal,[65] indicating the formation of Sn nanocrystals due to lithiation. Second, apart from the direct pathways for electron transfer from GF to SnO_2 nanorods, the conductive PANI shell can provide another route for electron transport, thus accelerating electron transport from active materials to the current collector, leading to the excellent rate capability. Finally, the 3D GF is undoubtedly beneficial to the electrochemical properties due to the high conductivity that enhance electron transport efficiency, the porous structure that facilitates the penetration of electrolyte, the high surface area that offers sufficient growth sites for SnO_2, and the low density that increases the gravimetric capacity of the electrode.

4. CONCLUSIONS

A unique 3D self-supported architecture consisting of SnO_2@PANI core−shell nanorod nanoarrays grown on macroporous graphite foam was successfully achieved via a facile solvothermal growth followed by electrochemical deposition. Benefiting from the synergetic effect of 3D porous GF that offers interconnected network with large specific area and high conductivity, 1D SnO_2 NRAs that provide direct pathways for electrons and decreased diffusion length for lithium ions, and the conductive PANI shell that accommodates the volume variation of SnO_2 and provides additional pathways for electron transport, the obtained binder-free, integrated GF@SnO_2 NRAs@PANI electrode for LIBs showed much enhanced electrochemical performance. Compared with the GF@SnO_2 NRAs electrode without the PANI layer, the GF@SnO_2 NRAs@PANI electrodes with a coating of the PANI layer exhibited significantly improved cycling performance and rate capability because the PANI shell not only facilitated electron transport, but also kept the integrity of the electrode. For the GF@SnO_2 NRAs@PANI-40 electrode with a PANI layer ~40 nm in thickness, a gravimetric capacity of 540 mAh g^{-1} with respect to the mass of the whole electrode was maintained after 50 cycles at 500 mA g^{-1}. Even at a high current density of 3 A

DOI: 10.1021/acsami.6b15880
ACS Appl. Mater. Interfaces 2017, 9, 9620−9629

g^{-1}, the electrode delivered a capacity of 414 mAh g^{-1}, indicating excellent rate capability. The GF@SnO_2 NRAs@PANI electrode represents a promising candidate for the integrated anodes potentially applicable in the next generation LIBs. The current synthetic strategy may open new pathways for constructing high-performance integrated electrodes based on the 3D GF substrate.

■ ASSOCIATED CONTENT

Supporting Information

The Supporting Information is available free of charge on the ACS Publications website at DOI: 10.1021/acsami.6b15880.

Additional TEM, SEM, TGA, and electrochemical characterization of the SnO_2-based nanocomposites (PDF)

■ AUTHOR INFORMATION

Corresponding Authors

*E-mail: liminqi@pku.edu.cn.
*E-mail: hhzhou@pku.edu.cn.

ORCID

Jin Zhang: 0000-0003-3731-8859
Limin Qi: 0000-0003-4959-6928

Notes

The authors declare no competing financial interest.

■ ACKNOWLEDGMENTS

This work was supported by NSFC (21473004 and 21673007) and MOST (2013CB932601).

■ REFERENCES

(1) Tarascon, J. M.; Armand, M. Issues and Challenges Facing Rechargeable Lithium Batteries. *Nature* **2001**, *414*, 359−367.
(2) Armand, M.; Tarascon, J. M. Building Better Batteries. *Nature* **2008**, *451*, 652−657.
(3) Larcher, D.; Tarascon, J. M. Towards Greener and More Sustainable Batteries for Electrical Energy Storage. *Nat. Chem.* **2015**, *7*, 19−29.
(4) Cabana, J.; Monconduit, L.; Larcher, D.; Palacin, M. R. Beyond Intercalation-Based Li-Ion Batteries: The State of The Art and Challenges of Electrode Materials Reacting Through Conversion Reactions. *Adv. Mater.* **2010**, *22*, E170−E192.
(5) Reddy, M. V.; Subba Rao, G. V.; Chowdari, B. V. Metal Oxides and Oxysalts as Anode Materials for Li Ion Batteries. *Chem. Rev.* **2013**, *113*, 5364−5457.
(6) Aravindan, V.; Lee, Y.-S.; Madhavi, S. Research Progress on Negative Electrodes for Practical Li-Ion Batteries: Beyond Carbonaceous Anodes. *Adv. Energy Mater.* **2015**, *5*, 1402225.
(7) Zhao, K.; Zhang, L.; Xia, R.; Dong, Y.; Xu, W.; Niu, C.; He, L.; Yan, M.; Qu, L.; Mai, L. SnO_2 Quantum Dots@Graphene Oxide as a High-Rate and Long-Life Anode Material for Lithium-Ion Batteries. *Small* **2016**, *12*, 588−594.
(8) Chen, J. S.; Lou, X. W. SnO_2-Based Nanomaterials: Synthesis and Application in Lithium-Ion Batteries. *Small* **2013**, *9*, 1877−1893.
(9) Huang, J. Y.; Zhong, L.; Wang, C. M.; Sullivan, J. P.; Xu, W.; Zhang, L. Q.; Mao, S. X.; Hudak, N. S.; Liu, X. H.; Subramanian, A.; Fan, H.; Qi, L.; Kushima, A.; Li, J. In Situ Observation of the Electrochemical Lithiation of a Single SnO_2 Nanowire Electrode. *Science* **2010**, *330*, 1515−1520.
(10) Xia, L.; Wang, S.; Liu, G.; Ding, L.; Li, D.; Wang, H.; Qiao, S. Flexible SnO_2/N-Doped Carbon Nanofiber Films as Integrated Electrodes for Lithium-Ion Batteries with Superior Rate Capacity and Long Cycle Life. *Small* **2016**, *12*, 853−859.
(11) Etacheri, V.; Seisenbaeva, G. A.; Caruthers, J.; Daniel, G.; Nedelec, J.-M.; Kessler, V. G.; Pol, V. G. Ordered Network of Interconnected SnO_2 Nanoparticles for Excellent Lithium-Ion Storage. *Adv. Energy Mater.* **2015**, *5*, 1401289.
(12) Kravchyk, K.; Protesescu, L.; Bodnarchuk, M. I.; Krumeich, F.; Yarema, M.; Walter, M.; Guntlin, C.; Kovalenko, M. V. Monodisperse and inorganically capped Sn and Sn/SnO_2 nanocrystals for high-performance Li-ion battery anodes. *J. Am. Chem. Soc.* **2013**, *135*, 4199−4202.
(13) Wang, H.; Rogach, A. L. Hierarchical SnO_2 Nanostructures: Recent Advances in Design, Synthesis, and Applications. *Chem. Mater.* **2014**, *26*, 123−133.
(14) Ye, J.; Zhang, H.; Yang, R.; Li, X.; Qi, L. Morphology-Controlled Synthesis of SnO_2 Nanotubes by Using 1D Silica Mesostructures as Sacrificial Templates and Their Applications in Lithium-Ion Batteries. *Small* **2010**, *6*, 296−306.
(15) Kim, H.; Cho, J. Hard Templating Synthesis of Mesoporous and Nanowire SnO_2 Lithium Battery Anode Materials. *J. Mater. Chem.* **2008**, *18*, 771−775.
(16) Wang, Z.; Luan, D.; Boey, F. Y.; Lou, X. W. Fast Formation of SnO_2 Nanoboxes with Enhanced Lithium Storage Capability. *J. Am. Chem. Soc.* **2011**, *133*, 4738−4741.
(17) Zhang, X.; Jiang, B.; Guo, J.; Xie, Y.; Tang, L. Large and Stable Reversible Lithium-Ion Storages From Mesoporous SnO_2 Nanosheets with Ultralong Lifespan Over 1000 Cycles. *J. Power Sources* **2014**, *268*, 365−371.
(18) Wang, D.; Yang, J.; Li, X.; Geng, D.; Li, R.; Cai, M.; Sham, T.-K.; Sun, X. Layer by Layer Assembly of Sandwiched Graphene/SnO_2 Nanorod/Carbon Nanostructures with Ultrahigh Lithium Ion Storage Properties. *Energy Environ. Sci.* **2013**, *6*, 2900−2906.
(19) Zhu, C.; Xia, X.; Liu, J.; Fan, Z.; Chao, D.; Zhang, H.; Fan, H. J. TiO_2 Nanotube@SnO_2 Nanoflake Core−Branch Arrays for Lithium-Ion Battery Anode. *Nano Energy* **2014**, *4*, 105−112.
(20) Xu, W.; Zhao, K.; Niu, C.; Zhang, L.; Cai, Z.; Han, C.; He, L.; Shen, T.; Yan, M.; Qu, L.; Mai, L. Heterogeneous Branched Core−Shell SnO_2−PANI Nanorod Arrays with Mechanical Integrity and Three Dimentional Electron Transport for Lithium Batteries. *Nano Energy* **2014**, *8*, 196−204.
(21) Zhang, L.; Zhao, K.; Xu, W.; Dong, Y.; Xia, R.; Liu, F.; He, L.; Wei, Q.; Yan, M.; Mai, L. Integrated SnO_2 Nanorod Array with Polypyrrole Coverage For High-Rate and Long-Life Lithium Batteries. *Phys. Chem. Chem. Phys.* **2015**, *17*, 7619−7623.
(22) Cao, Z.; Yang, H.; Dou, P.; Wang, C.; Zheng, J.; Xu, X. Synthesis of Three-Dimensional Hollow SnO_2@PPy Nanotube Arrays via Template-Assisted Method and Chemical Vapor-Phase Polymerization as High Performance Anodes for Lithium-Ion Batteries. *Electrochim. Acta* **2016**, *209*, 700−708.
(23) Ma, X.; Luo, W.; Yan, M.; He, L.; Mai, L. In situ Characterization of Electrochemical Processes in One Dimensional Nanomaterials for Energy Storages Devices. *Nano Energy* **2016**, *24*, 165−188.
(24) Zhou, D.; Song, W.; Fan, L. Hollow Core−Shell SnO_2/C Fibers as Highly Stable Anodes for Lithium-Ion Batteries. *ACS Appl. Mater. Interfaces* **2015**, *7*, 21472−21478.
(25) Zhang, M.; Sun, Z.; Zhang, T.; Sui, D.; Ma, Y.; Chen, Y. Excellent Cycling Stability with High SnO_2 Loading on A Three-Dimensional Graphene Network for Lithium Ion Batteries. *Carbon* **2016**, *102*, 32−38.
(26) Huang, Y.; Wu, D.; Jiang, J.; Mai, Y.; Zhang, F.; Pan, H.; Feng, X. Highly Oriented Macroporous Graphene Hybrid Monoliths for Lithium Ion Battery Electrodes with Ultrahigh Capacity andRate Capability. *Nano Energy* **2015**, *12*, 287−295.
(27) Cong, H.-P.; Xin, S.; Yu, S.-H. Flexible Nitrogen-Doped Graphene/SnO_2 Foams Promise Kinetically Stable Lithium Storage. *Nano Energy* **2015**, *13*, 482−490.
(28) Li, Y.; Zhang, H.; Kang Shen, P. Ultrasmall Metal Oxide Nanoparticles Anchored on Three-Dimensional Hierarchical Porous Gaphene-Like Networks as Anode for High-Performance Lithium Ion Batteries. *Nano Energy* **2015**, *13*, 563−572.

(29) Zhang, Z.; Wang, L.; Xiao, J.; Xiao, F.; Wang, S. One-Pot Synthesis of Three-Dimensional Graphene/Carbon Nanotube/SnO_2 Hybrid Architectures with Enhanced Lithium Storage Properties. *ACS Appl. Mater. Interfaces* **2015**, *7*, 17963−17968.
(30) Yao, X.; Guo, G.; Ma, X.; Zhao, Y.; Ang, C. Y.; Luo, Z.; Nguyen, K. T.; Li, P. Z.; Yan, Q.; Zhao, Y. In Situ Integration of Anisotropic SnO_2 Heterostructures inside Three-Dimensional Graphene Aerogel for Enhanced Lithium Storage. *ACS Appl. Mater. Interfaces* **2015**, *7*, 26085−26093.
(31) Tian, R.; Zhang, Y.; Chen, Z.; Duan, H.; Xu, B.; Guo, Y.; Kang, H.; Li, H.; Liu, H. The Effect of Annealing on A 3D SnO_2/Graphene Foam as an Advanced Lithium-Ion Battery Anode. *Sci. Rep.* **2016**, *6*, 19195.
(32) Zhou, D.; Song, W.; Li, X.; Fan, L. Hierarchical Porous Reduced Graphene Oxide/SnO_2 Networks as Highly Stable Anodes for Lithium-Ion Batteries. *Electrochim. Acta* **2016**, *207*, 9−15.
(33) Guo, J. X.; Jiang, B.; Zhang, X.; Liu, H. Monodisperse SnO_2 Anchored reduced Graphene Oxide Nanocomposites as Negative Electrode with High Rate Capability and Long Cyclability for Lithium-Ion Batteries. *J. Power Sources* **2014**, *262*, 15−22.
(34) Ellis, B. L.; Knauth, P.; Djenizian, T. Three-Dimensional Self-Supported Metal Oxides for Advanced Energy Storage. *Adv. Mater.* **2014**, *26*, 3368−3397.
(35) Zhang, F.; Qi, L. Recent Progress in Self-Supported Metal Oxide Nanoarray Electrodes for Advanced Lithium-Ion Batteries. *Adv. Sci.* **2016**, *3*, 1600049.
(36) Hu, R.; Zhang, H.; Liu, J.; Chen, D.; Yang, L.; Zhu, M.; Liu, M. Deformable Fibrous Carbon Supported Ultrafine Nano-SnO_2 as A High Volumetric Capacity and Cyclic Durable Anode for Li Storage. *J. Mater. Chem. A* **2015**, *3*, 15097−15107.
(37) Botas, C.; Carriazo, D.; Singh, G.; Rojo, T. Sn− and SnO_2− Graphene Flexible Foams Suitable as Binder-Free Anodes for Lithium Ion Batteries. *J. Mater. Chem. A* **2015**, *3*, 13402−13410.
(38) Liang, J.; Zhao, Y.; Guo, L.; Li, L. Flexible Free-Standing Graphene/SnO_2 Nanocomposites Paper for Li-Ion Battery. *ACS Appl. Mater. Interfaces* **2012**, *4*, 5742−5748.
(39) Noerochim, L.; Wang, J. Z.; Chou, S.-L.; Wexler, D.; Liu, H.-K. Free-Standing Single-Walled Carbon Nanotube/SnO_2 Anode Paper for Flexible Lithium-Ion Batteries. *Carbon* **2012**, *50*, 1289−1297.
(40) Dirican, M.; Yanilmaz, M.; Fu, K.; Lu, Y.; Kizil, H.; Zhang, X. Carbon-Enhanced Electrodeposited SnO_2/Carbon Nanofiber Composites as Anode for Lithium-Ion Batteries. *J. Power Sources* **2014**, *264*, 240−247.
(41) Ma, Y.; Asfaw, H. D.; Edström, K. Three-Dimensional Carbon Foam Supported Tin Oxide Nanocrystallites with Tunable Size Range: Sulfonate Anchoring Synthesis and High Rate Lithium Storage Properties. *J. Power Sources* **2015**, *294*, 208−215.
(42) Jiang, S.; Zhao, B.; Ran, R.; Cai, R.; Tadé, M. O.; Shao, Z. A Freestanding Composite Film Electrode Stacked from Hierarchical Electrospun SnO_2 Nanorods and Graphene Sheets for Reversible Lithium Storage. *RSC Adv.* **2014**, *4*, 9367−9371.
(43) Hu, G.; Xu, C.; Sun, Z.; Wang, S.; Cheng, H. M.; Li, F.; Ren, W. 3D Graphene-Foam-Reduced-Graphene-Oxide Hybrid Nested Hierarchical Networks for High-Performance Li-S Batteries. *Adv. Mater.* **2016**, *28*, 1603−1609.
(44) Ji, H.; Zhang, L.; Pettes, M. T.; Li, H.; Chen, S.; Shi, L.; Piner, R.; Ruoff, R. S. Ultrathin graphite foam: A Three-Dimensional Conductive Network for Battery Electrodes. *Nano Lett.* **2012**, *12*, 2446−2451.
(45) Xia, X.; Chao, D.; Fan, Z.; Guan, C.; Cao, X.; Zhang, H.; Fan, H. J. A New Type of Porous Graphite Foams and Their Integrated Composites with Oxide/Polymer Core/Shell Nanowires for Supercapacitors: Structural Design, Fabrication, And Full Supercapacitor Demonstrations. *Nano Lett.* **2014**, *14*, 1651−1658.
(46) Ji, J.; Ji, H.; Zhang, L. L.; Zhao, X.; Bai, X.; Fan, X.; Zhang, F.; Ruoff, R. S. Graphene-Encapsulated Si on Ultrathin-Graphite Foam as Anode for High Capacity Lithium-Ion Batteries. *Adv. Mater.* **2013**, *25*, 4673−4677.
(47) Wang, J.; Liu, J.; Chao, D.; Yan, J.; Lin, J.; Shen, Z. X. Self-Assembly of Honeycomb-Like MoS2 Nanoarchitectures Anchored into Graphene Foam for Enhanced Lithium-Ion Storage. *Adv. Mater.* **2014**, *26*, 7162−7169.
(48) Luo, J.; Liu, J.; Zeng, Z.; Ng, C. F.; Ma, L.; Zhang, H.; Lin, J.; Shen, Z.; Fan, H. J. Three-Dimensional Graphene Foam Supported Fe_3O_4 Lithium Battery Anodes with Long Cycle Life and High Rate Capability. *Nano Lett.* **2013**, *13*, 6136−6143.
(49) Deng, J.; Chen, L.; Sun, Y.; Ma, M.; Fu, L. Interconnected MnO_2 Nanoflakes Assembled on Graphene Foam as A Binder-Free and Long-Cycle Life Lithium Battery Anode. *Carbon* **2015**, *92*, 177−184.
(50) Chen, S.; Wang, M.; Ye, J.; Cai, J.; Ma, Y.; Zhou, H.; Qi, L. Kinetics-Controlled Growth of Aligned Mesocrystalline SnO_2 Nanorod Arrays for Lithium-Ion Batteries with Superior Rate Performance. *Nano Res.* **2013**, *6*, 243−252.
(51) Chen, S.; Xin, Y.; Zhou, Y.; Zhang, F.; Ma, Y.; Zhou, H.; Qi, L. Branched CNT@SnO_2 Nanorods@Carbon Hierarchical Heterostructures for Lithium Ion Batteries with High Reversibility and Rate Capability. *J. Mater. Chem. A* **2014**, *2*, 15582−15589.
(52) Ma, W.; Zhang, F.; Li, L.; Chen, S.; Qi, L.; Liu, H.; Bai, Y. Facile Synthesis of Mesocrystalline SnO_2 Nanorods on Reduced Graphene Oxide Sheets: An Appealing Multifunctional Affinity Probe for Sequential Enrichment of Endogenous Peptides and Phosphopeptides. *ACS Appl. Mater. Interfaces* **2016**, *8*, 35099−35105.
(53) Jeong, J. M.; Choi, B. G.; Lee, S. C.; Lee, K. G.; Chang, S. J.; Han, Y. K.; Lee, Y. B.; Lee, H. U.; Kwon, S.; Lee, G.; Lee, C. S.; Huh, Y. S. Hierarchical Hollow Spheres of Fe_2O_3 @Polyaniline for Lithium Ion Battery Anodes. *Adv. Mater.* **2013**, *25*, 6250−6255.
(54) Lepage, D.; Michot, C.; Liang, G.; Gauthier, M.; Schougaard, S. B. A Soft Chemistry Approach to Coating of $LiFePO_4$ with a Conducting Polymer. *Angew. Chem., Int. Ed.* **2011**, *50*, 6884−6887.
(55) Li, W.; Zhang, Q.; Zheng, G.; Seh, Z. W.; Yao, H.; Cui, Y. Understanding the Role of Different Conductive Polymers in Improving The Nanostructured Sulfur Cathode Performance. *Nano Lett.* **2013**, *13*, 5534−5540.
(56) Chao, D.; Xia, X.; Liu, J.; Fan, Z.; Ng, C. F.; Lin, J.; Zhang, H.; Shen, Z. X.; Fan, H. J. A V_2O_5/Conductive-Polymer Core/Shell Nanobelt Array on Three-Dimensional Graphite Foam: A High-Rate, Ultrastable, and Freestanding Cathode for Lithium-Ion Batteries. *Adv. Mater.* **2014**, *26*, 5794−5800.
(57) Chen, Z.; Ren, W.; Gao, L.; Liu, B.; Pei, S.; Cheng, H. M. Three-Dimensional Flexible and Conductive Interconnected Graphene Networks Grown by Chemical Vapour Deposition. *Nat. Mater.* **2011**, *10*, 424−428.
(58) Wang, H.; Wang, Y.; Cao, X.; Feng, M.; Lan, G. Vibrational Properties of Graphene and Graphene Layers. *J. Raman Spectrosc.* **2009**, *40*, 1791−1796.
(59) Lee, G. H.; Lee, J. W.; Choi, J. I. L.; Kim, S. J.; Kim, Y.-H.; Kang, J. K. Ultrafast Discharge/Charge Rate and Robust Cycle Life for High-Performance Energy Storage Using Ultrafine Nanocrystals on the Binder-Free Porous Graphene Foam. *Adv. Funct. Mater.* **2016**, *26*, 5139−5148.
(60) Tawale, J. S.; Gupta, G.; Mohan, A.; Kumar, A.; Srivastava, A. K. Growth of Thermally Evaporated SnO_2 Nanostructures for Optical and Humidity Sensing Application. *Sens. Actuators, B* **2014**, *201*, 369−377.
(61) Lindfors, T.; Kvarnstrom, C.; Ivaska, A. Raman and UV−vis Spectroscopic Study of Polyaniline Membranes Containing a Bulky Cationic Additive. *J. Electroanal. Chem.* **2002**, *518*, 131−138.
(62) Zhou, X.; Wan, L. J.; Guo, Y. G. Binding SnO_2 Nanocrystals in Nitrogen-Doped Graphene Sheets as Anode Materials for Lithium-Ion Batteries. *Adv. Mater.* **2013**, *25*, 2152−2157.
(63) Zhang, Y. C.; You, Y.; Xin, S.; Yin, Y. X.; Zhang, J.; Wang, P.; Zheng, X. S.; Cao, F. F.; Guo, Y.-G. Rice Husk-Derived Hierarchical Silicon/Nitrogen-Doped Carbon/Carbon Nanotube Spheres as Low-Cost and High-Capacity Anodes for Lithium-Ion Batteries. *Nano Energy* **2016**, *25*, 120−127.

DOI: 10.1021/acsami.6b15880
ACS Appl. Mater. Interfaces 2017, 9, 9620−9629

(64) Wu, X. L.; Guo, Y. G.; Su, J.; Xiong, J. W.; Zhang, Y. L.; Wan, L. J. Carbon-Nanotube-Decorated Nano-LiFePO4@C Cathode Material with Superior High-Rate and Low-Temperature Performances for Lithium-Ion Batteries. *Adv. Energy Mater.* **2013**, *3*, 1155−1160.
(65) Qin, J.; He, C.; Zhao, N.; Wang, Z.; Shi, C.; Liu, E.; Li, J. Graphene Networks Anchored with Sn@Graphene as Lithium Ion Battery Anode. *ACS Nano* **2014**, *8*, 1728−1738.

DOI: 10.1021/acsami.6b15880
ACS Appl. Mater. Interfaces 2017, 9, 9620−9629